The Astrophysical Journal, 841:129 (14pp), 2017 June 1 https://doi.org/10.3847/1538-4357/aa72e3

Hanle-Zeeman Scattering Matrix for Magnetic Dipole Transitions

A. Megha[1], M. Sampoorna[1], K. N. Nagendra[1], and K. Sankarasubramanian[1,2,3]
[1] Indian Institute of Astrophysics, Koramangala, Bengaluru 560 034, India
megha@iiap.res.in, sampoorna@iiap.res.in, knn@iiap.res.in, sankar@iiap.res.in
[2] Space Astronomy group, ISRO Satellite Centre, Bengaluru, India
[3] CESSI, IISER, Kolkata, India
Received 2017 March 8; revised 2017 May 8; accepted 2017 May 10; published 2017 June 5

Abstract

The polarization of the light that is scattered by the coronal ions is influenced by the anisotropic illumination from the photosphere and the magnetic field structuring in the solar corona. The properties of the coronal magnetic fields can be well studied by understanding the polarization properties of coronal forbidden emission lines that arise from magnetic dipole ($M1$) transitions in the highly ionized atoms that are present in the corona. We present the classical scattering theory of the forbidden lines for a more general case of arbitrary-strength magnetic fields. We derive the scattering matrix for $M1$ transitions using the classical magnetic dipole model of Casini & Lin and applying the scattering matrix approach of Stenflo. We consider a two-level atom model and neglect collisional effects. The scattering matrix so derived is used to study the Stokes profiles formed in coronal conditions in those regions where the radiative excitations dominate collisional excitations. To this end, we take into account the integration over a cone of an unpolarized radiation from the solar disk incident on the scattering atoms. Furthermore, we also integrate along the line of sight to calculate the emerging polarized line profiles. We consider radial and dipole magnetic field configurations and spherically symmetric density distributions. For our studies we adopt the atomic parameters corresponding to the [Fe XIII] 10747 Å coronal forbidden line. We also discuss the nature of the scattering matrix for $M1$ transitions and compare it with that for the electric dipole ($E1$) transitions.

Key words: atomic processes – line: formation – polarization – Sun: atmosphere – Sun: corona – Sun: magnetic fields

1. Introduction

The plasma β values being low in the inner corona of the Sun suggests that the magnetic fields emerging from subphotospheric layers control the dynamics and heating of the corona. Our ability to determine the properties of the coronal magnetic fields remains severely limited because the fields in the quiet-Sun corona are intrinsically weak. The influence of these fields on the electromagnetic radiation that is emitted by the coronal plasma is accordingly weak. One of the best ways to determine the properties of coronal magnetic fields is to study the polarization properties of coronal forbidden emission lines that are produced as the result of an anisotropic excitation of the ions that are present in the corona (see Figure 1). The quest for understanding the origin and formation of coronal emission line polarization dates back to the early part of the twentieth century. The first attempt to measure the polarization in coronal lines, especially the green forbidden emission line (5303 Å), was made by Wood (1905). He reported that the polarization is lower than 1%. Öhman (1929) was the first to mention that the coronal lines might be polarized, but there was lack of information regarding the origin of the polarization in these lines. The first theoretical analysis of coronal emission line polarization was given by Charvin (1965, see also Hyder 1965), who studied the detailed interaction of anisotropic photospheric light with the radiating ions and showed how the linear polarization is related to the direction of the magnetic field projected onto the plane of the sky (POS). House (1972) represents an important landmark in the theoretical calculation of the polarization of coronal forbidden lines. His treatment was restricted to pure scattering. Sahal-Bréchot (1974, 1977) and House (1977) included the collisional terms in the statistical equilibrium equation for the radiating atom. Based on the statistical equilibrium solutions of Sahal-Bréchot (1977) and House (1977) for the [Fe XIII] 10747 Å line, a simple analytic form was deduced by Querfeld (1982), which shows an explicit dependence of the Stokes vector on coronal electron density, magnetic field direction, and temperature. However, the circular polarization was neglected in the above-mentioned theoretical works. Casini & Judge (1999) provided a consistent theory treating both linear and circular polarizations of $M1$ lines. They also gave a generalized magnetograph formula for determining the longitudinal component of the vector magnetic field. Based on this theory, Judge & Casini (2001) developed a diagnostic code called Coronal Line Emission, which is employed by Gibson et al. (2016) in a community resource toolset, namely FORWARD. It is extensively used for magnetic field modeling and other studies of the solar corona.

A classical oscillator model for the magnetic dipoles was proposed by Casini & Lin (2002). Their model is based on a 3D L–C circuit analogy, which considers the magnetic field component of the incident radiation that induces the magnetic dipole ($M1$) transitions. Based on this model, Lin & Casini (2000) derived the polarization properties of the coronal forbidden emission lines in the collisionless regime. They particularly considered the case of the strong-field (or saturated Hanle) regime, wherein the Larmor frequency is much larger than the natural width of the line. Their classical result coincides with the quantum mechanical result derived in Casini & Judge (1999) in the restricted case of the $J = 0 \rightarrow 1 \rightarrow 0$ transition. Stenflo (1998, hereafter called S98) presented a general approach to derive the Hanle-Zeeman scattering matrix for the electric dipole ($E1$) transitions. In the present paper, starting from the solution of the classical damped $M1$ oscillator (Casini & Lin 2002), we derive the Hanle-Zeeman scattering

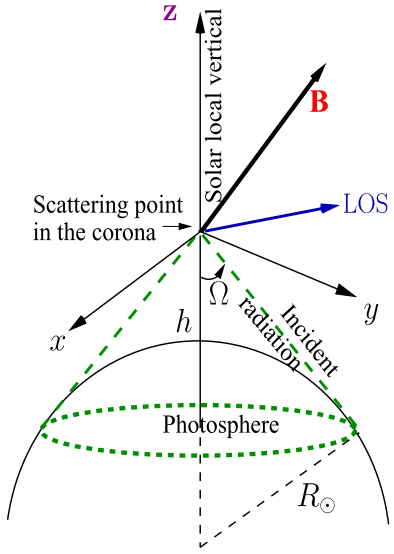

Figure 1. Geometry describing the anisotropic illumination of ions in the corona by the photospheric radiation field.

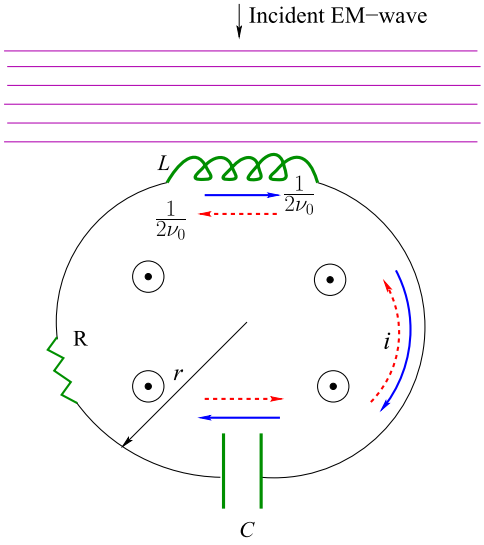

Figure 2. Plane circular L–R–C circuit irradiated by a monochromatic electromagnetic plane wave. This circuit represents a one-dimensional $M1$ oscillator when we consider the interaction of the circuit with the magnetic field component of the electromagnetic radiation incident from the top. The applied external magnetic field is perpendicular to the plane of the paper.

matrix following the approach of S98. We consider coherent scattering in arbitrary-strength magnetic fields and a two-level atom with the $J = 0 \rightarrow 1 \rightarrow 0$ $M1$ transition. The scattering matrix for the coronal forbidden emission lines is retrieved from this general theory as a limiting case (strong-field limit). The effects of collisions and multilevel coupling are neglected in our formalism. Therefore the present approach can be applied only to those regions in the corona where radiative excitations of ions are dominant.

The paper is organized as follows. In Sections 2 and 3 we derive the Jones scattering matrix and Mueller scattering matrix using the S98 approach. In Section 4 the Hanle-Zeeman scattering matrix for $M1$ transitions derived using S98 approach is expressed in terms of the irreducible spherical tensors of Landi Degl'Innocenti (1984) and the generalized profile functions defined by Landi Degl'Innocenti et al. (1991). In Section 5 we describe a procedure to perform angular integration over the unpolarized incident radiation from the solar photosphere. The resulting Stokes profiles from the scattering point are also presented. In Section 6 we consider the so-called "line-of-sight integration" and present emerging Stokes profiles for radial and dipole field distributions within the corona. Conclusions are presented in Section 7.

2. Jones Scattering Matrix for $M1$ Transitions

Here we derive the scattering amplitudes for the $M1$ transitions using the Jones calculus. For this we use a classical model for the damped, magnetic dipole oscillator proposed by Casini & Lin (2002). In this model they have considered a plane, circular L–C circuit with no applied electromotive force (EMF) that is irradiated by a monochromatic electromagnetic plane wave with its magnetic field component varying as $\boldsymbol{B}_{\rm in}(t) = \boldsymbol{B}_0 \exp(-i\omega t)$. Here the dipole approximation is introduced by assuming that the radius of the L–C circuit r is much smaller than the wavelength of the incident radiation ($r \ll 2\pi c/\omega$). Because the net magnetic flux through the circuit includes flux due to radiation reaction current, the circuit behaves as an L–R–C circuit (see Figure 2). Using the theory of quasi-stationary currents (see Casini & Lin 2002 for details), the idea of L–R–C circuit is extended to three dimensions to construct a classical $M1$ oscillator model to represent an atomic system. Thus the atomic system is now schematized by considering the three atomic $M1$ oscillators describing the forbidden transition, $J = 0 \rightarrow 1 \rightarrow 0$, as three plane circular L–R–C circuits, oscillating orthogonally (so that the mutual inductance between the circuits can be neglected), and rigidly oriented with respect to some Cartesian basis $\boldsymbol{e}_x, \boldsymbol{e}_y, \boldsymbol{e}_z$. A homogeneous stationary external magnetic field $\boldsymbol{B} = B\boldsymbol{e}_z$ is applied to this 3D physical system. As a consequence, each circuit in the atomic model will generally be subjected to a torque. After some algebra, the complete oscillator equation for the classical damped $M1$ oscillator is obtained as

$$\ddot{\boldsymbol{m}} + \gamma\dot{\boldsymbol{m}} + 2\omega_B\,\dot{\boldsymbol{m}} \times \boldsymbol{e}_z + \omega_0^2\boldsymbol{m} = \frac{\omega^2\sigma^2}{c^2 L}\boldsymbol{B}_{\rm in}, \qquad (1)$$

where $\boldsymbol{m}$ is the magnetic dipole associated with the three circuits, L is the inductance, $\gamma = R/L$ is the damping constant with R being the resistance, σ is the area of the circuit, $\omega_0 \approx 1/LC$ is the characteristic resonance frequency of the L–R–C circuit, and ω_B is the Larmor frequency. This equation is analogous to the corresponding damped electric dipole oscillator equation given in Equation (3.33) of Stenflo (1994, hereafter called S94). The only difference is that the driving force in Equation (1) for the magnetic dipole is the magnetic vector component of the incident electromagnetic radiation, while it is the electric vector component for the electric dipole oscillator. Equation (1) decouples in the basis of spherical unit vectors, and the resulting solution in component form is given by

$$m_q(\omega) = \frac{\omega^2\sigma^2}{c^2 L}\frac{B_q^{\rm in}}{\omega_0^2 - \omega^2 - 2q\omega\omega_B - {\rm i}\gamma\omega}, \qquad (2)$$

where $q = 0, \pm 1$ and $B_q^{\rm in}$ is the spherical component of the incident radiation. Hereafter we refer to the magnetic field of the electromagnetic radiation as the radiation magnetic field.

For a spectral line, $\omega \simeq \omega_0$ is satisfied and therefore $|\omega_0 - \omega| \ll \omega_0$. This condition simplifies the resonant term in Equation (2) as

$$\frac{1}{\omega_0^2 - \omega^2 - 2q\omega\omega_B - \mathrm{i}\gamma\omega} \approx \frac{1/2\omega_0}{[\omega_0 - \omega - q\omega_B - \mathrm{i}\gamma/2]}. \quad (3)$$

Following Bommier & Stenflo (1999), we now define the area normalized profile function Φ_q as

$$\Phi_q = \frac{2/\mathrm{i}}{\omega_0 - \omega - q\omega_B - \mathrm{i}\gamma/2}. \quad (4)$$

Thus Equation (2) can be rewritten as

$$m_q(\omega) \sim \Phi_q B_q^{\mathrm{in}}. \quad (5)$$

We denote the spherical components of the scattered radiation magnetic field as B_q^{out}, which is proportional to the spherical components of the magnetic dipole vector amplitude m_q. Following S94, we can write $B_q = \sum_\alpha \varepsilon_q^\alpha B_\alpha$, where $\alpha = 1, 2$ are the linear polarization basis vectors and ε_q^α are the spherical vector components of the linear unit vector $\boldsymbol{e}_\alpha$. Thus the scattered radiation magnetic field can now be written as

$$B_\alpha^{\mathrm{out}} = \sum_q \varepsilon_q^{\alpha *} B_q^{\mathrm{out}} \sim \sum_q \varepsilon_q^{\alpha *} \Phi_q B_q^{\mathrm{in}}. \quad (6)$$

Simplifying further by a substitution for $B_q^{\mathrm{in}} = \sum_\beta \varepsilon_q^\beta B_\beta^{\mathrm{in}}$, we obtain

$$B_\alpha^{\mathrm{out}} = \sum_\beta w_{\alpha\beta}^B B_\beta^{\mathrm{in}}, \quad (7)$$

where

$$w_{\alpha\beta}^B = \sum_q \varepsilon_q^{\alpha *} \varepsilon_q^\beta \Phi_q, \quad (8)$$

are the components of the 2×2 Jones scattering matrix $\boldsymbol{w^B}$, which describes the interaction of radiation with the medium. The quantity $w_{\alpha\beta}^B$ given above has exactly the same form as that for the electric dipole transitions. However, it is derived considering the radiation magnetic field. Because the Stokes parameters are defined on the basis of the electric field components of the radiation, we also transform Equation (7) to the same basis. This can be achieved by using the relation between the radiation electric and magnetic field vectors, which is given by $\boldsymbol{E} = \boldsymbol{B} \times \hat{\boldsymbol{r}}$. Thus the relation between the radiation electric and magnetic field vectors ($\boldsymbol{B} = -E_2\boldsymbol{e}_1 + E_1\boldsymbol{e}_2$) can be written in matrix form as

$$\boldsymbol{E} = \boldsymbol{\alpha B}; \quad \boldsymbol{B} = \boldsymbol{\alpha}^\dagger \boldsymbol{E}, \quad (9)$$

where

$$\boldsymbol{\alpha} = \begin{pmatrix} 0 & 1 \\ -1 & 0 \end{pmatrix}, \boldsymbol{\alpha}^\dagger = \begin{pmatrix} 0 & -1 \\ 1 & 0 \end{pmatrix}. \quad (10)$$

Using the above relation, Equation (7) can be rewritten in matrix form as

$$\boldsymbol{E}^{\mathrm{out}} = \boldsymbol{w^E E}^{\mathrm{in}}, \quad (11)$$

where

$$\boldsymbol{w^E} = \boldsymbol{\alpha w^B \alpha}^\dagger, \quad (12)$$

which is now defined using the radiation electric field vector.

3. Scattering Matrix for $M1$ Transitions

The Mueller scattering matrix $\boldsymbol{M}^{M1}$, which describes the transformation from incident to the scattered Stokes vectors, is given by

$$\boldsymbol{M}^{M1} = \boldsymbol{T W}^{M1} \boldsymbol{T}^{-1}, \quad (13)$$

where

$$\boldsymbol{W}^{M1} = \boldsymbol{w^E} \otimes \boldsymbol{w^{E*}}. \quad (14)$$

The matrices $\boldsymbol{T}$, $\boldsymbol{T}^{-1}$ are mathematical transformation matrices and are given by

$$\boldsymbol{T} = \begin{pmatrix} 1 & 0 & 0 & 1 \\ 1 & 0 & 0 & -1 \\ 0 & 1 & 1 & 0 \\ 0 & -\mathrm{i} & \mathrm{i} & 0 \end{pmatrix}, \quad (15)$$

$$\boldsymbol{T}^{-1} = \frac{1}{2}\begin{pmatrix} 1 & 1 & 0 & 0 \\ 0 & 0 & 1 & \mathrm{i} \\ 0 & 0 & 1 & -\mathrm{i} \\ 1 & -1 & 0 & 0 \end{pmatrix}. \quad (16)$$

The tensor product in Equation (14) has the same form as given in Equation (10) of S98, but with $\boldsymbol{w}$ there replaced by $\boldsymbol{w^E}$ defined in Equation (12). In terms of the elements of $\boldsymbol{w^B}$, the tensor product in Equation (14) can be written as

$$\boldsymbol{W}^{M1} = \begin{pmatrix} w_{22}^B w_{22}^{B*} & -w_{22}^B w_{21}^{B*} & -w_{21}^B w_{22}^{B*} & w_{21}^B w_{21}^{B*} \\ -w_{22}^B w_{12}^{B*} & w_{22}^B w_{11}^{B*} & w_{21}^B w_{12}^{B*} & -w_{21}^B w_{11}^{B*} \\ -w_{12}^B w_{22}^{B*} & w_{12}^B w_{21}^{B*} & w_{11}^B w_{22}^{B*} & -w_{11}^B w_{21}^{B*} \\ w_{12}^B w_{12}^{B*} & -w_{12}^B w_{11}^{B*} & -w_{11}^B w_{12}^{B*} & w_{11}^B w_{11}^{B*} \end{pmatrix}. \quad (17)$$

Comparing Equation (10) of S98 with Equation (17), one can clearly see the role played by $\boldsymbol{\alpha}$ and $\boldsymbol{\alpha}^\dagger$ (namely the change of signs as well as the changed positions of the elements in the matrix $\boldsymbol{W}^{M1}$ with respect to the matrix $\boldsymbol{W}$ defined in Equation (10) of S98). Since $\boldsymbol{w^B}$ is identical to $\boldsymbol{w}$ corresponding to electric dipole transitions (namely that of S98), following S98 (see his Equation (12)), we define

$$\begin{aligned} A &= |w_{11}^B|^2, & B &= |w_{22}^B|^2, \\ C &= |w_{12}^B|^2, & D &= |w_{21}^B|^2, \\ a &= w_{11}^B w_{22}^{B*}, & b &= w_{11}^B w_{12}^{B*}, \\ c &= w_{11}^B w_{21}^{B*}, & d &= w_{12}^B w_{21}^{B*}, \\ e &= w_{12}^B w_{22}^{B*}, & f &= w_{21}^B w_{22}^{B*}. \end{aligned} \quad (18)$$

With these quantities the Mueller matrix for the magnetic dipole transitions can be organized as

$$\boldsymbol{M}^{M1} = \boldsymbol{M}_Q^{M1} + \Re(\boldsymbol{M}_U^{M1}) + \Im(\boldsymbol{M}_V^{M1}), \quad (19)$$

where

$$\boldsymbol{M}_{Q}^{M1} = \frac{1}{2} \times \begin{pmatrix} A+B+C+D & -(A-B-C+D) & 0 & 0 \\ -(A-B+C-D) & A+B-C-D & 0 & 0 \\ 0 & 0 & 0 & 0 \\ 0 & 0 & 0 & 0 \end{pmatrix},$$

$$\boldsymbol{M}_{U}^{M1} = \begin{pmatrix} 0 & 0 & -(b+f) & 0 \\ 0 & 0 & b-f & 0 \\ -(c+e) & c-e & a+d & 0 \\ 0 & 0 & 0 & a-d \end{pmatrix},$$

$$\boldsymbol{M}_{V}^{M1} = \begin{pmatrix} 0 & 0 & 0 & -b-f \\ 0 & 0 & 0 & -(-b+f) \\ 0 & 0 & 0 & -(-a+d) \\ c+e & -(c-e) & -(a+d) & 0 \end{pmatrix}. \quad (20)$$

Comparing the elements of $\boldsymbol{M}^{M1}$ given in Equation (20) with the corresponding elements in Equation (14) of S98, we see that the Mueller matrix for magnetic dipole transitions is exactly the same as that for the electric dipole transitions, except for the change in the signs of certain elements. These elements that have undergone sign change are $\boldsymbol{M}_{Q,12}^{M1}$, $\boldsymbol{M}_{Q,21}^{M1}$, $\boldsymbol{M}_{U,13}^{M1}$, $\boldsymbol{M}_{U,31}^{M1}$, $\boldsymbol{M}_{V,24}^{M1}$, $\boldsymbol{M}_{V,42}^{M1}$, $\boldsymbol{M}_{V,34}^{M1}$, and $\boldsymbol{M}_{V,43}^{M1}$. The analytical form of the Hanle-Zeeman scattering matrix for $J = 0 \rightarrow 1 \rightarrow 0$ $M1$ transition in the magnetic reference frame (MRF–namely, magnetic field along the z-axis) can be derived following Section 4 of S98. Indeed, the expressions turn out to be identical to those given in Section 4 of S98, with the sign changes already mentioned above. All the special cases discussed in Section 5 of S98 can also be recovered for the $M1$ transitions. In the following subsection we particularly discuss the strong-field regime of the Hanle effect, which is of relevance to coronal forbidden emission lines.

3.1. Saturated Hanle Regime

For the coronal forbidden lines, the Einstein spontaneous emission coefficient A is very small (typically, $A \sim 10\ \mathrm{s}^{-1}$). Therefore excited states of these forbidden lines have extraordinarily long lifetimes, due to which the natural line widths of these lines are very small compared to the Zeeman splitting even for microgauss fields. As the expected field strengths for the quiet-Sun corona are much stronger ($\sim$10 G), for these lines $\omega_B \gg A$. Thus we are always in the saturated Hanle regime (or strong-field regime with respect to the traditional Hanle effect) in forbidden lines in the solar corona. Under this condition the separated magnetic substates of the upper level do not interfere and scatter the incident radiation incoherently (independently). The tensor product defined in Equation (14) has terms of the type $w_{\alpha\beta}^{B} w_{\alpha'\beta'}^{B*}$. This involves a coherent summation over q, q' (see Equation (8)). In the saturated Hanle regime we neglect the interference terms. In other words, an incoherent summation is performed ($q = q'$) when forming the tensor product. Thus the Mueller matrix for the coronal forbidden lines under the saturated Hanle regime is given by

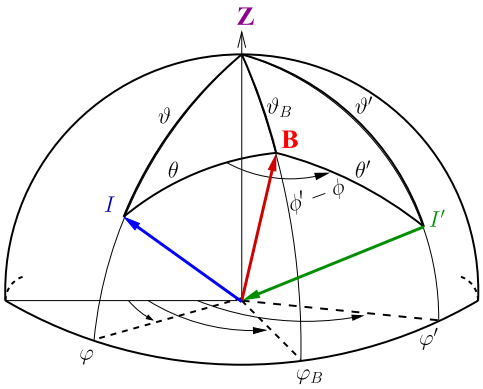

Figure 3. Geometry showing the scattering process in a coordinate system where the magnetic field makes an angle ϑ_B with respect to the polar Z-axis and has an azimuth of φ_B . We refer to this as the atmospheric reference frame. In this frame (ϑ', φ') refer to the incident ray, and (ϑ, φ) to the scattered ray. (θ', ϕ') refer to the incident ray, and (θ, ϕ) to the scattered ray with respect to the magnetic field (magnetic reference frame).

$$\boldsymbol{M}_{\mathrm{corona}}^{M1}/H_0 = \boldsymbol{E}_{11} + \frac{3}{8} \begin{pmatrix} \frac{1}{3}(1-3\mu^2)(1-3\mu'^2) & -(1-3\mu^2)(1-\mu'^2) & 0 & 0 \\ -(1-\mu^2)(1-3\mu'^2) & 3(1-\mu^2)(1-\mu'^2) & 0 & 0 \\ 0 & 0 & 0 & 0 \\ 0 & 0 & 0 & 4\mu\mu' \end{pmatrix}. \quad (21)$$

In the above equation $\mu = \cos\theta$, $\mu' = \cos\theta'$, where θ and θ' are the colatitudes of the scattered and incident radiation (see Figure 3). Since the Zeeman splitting for the coronal forbidden lines is much smaller than the Doppler width, the Voigt functions for $q = \pm 1$ are taken as H_0 (namely, $H_{\pm} \approx H_0$). The notations used in the above expression are the same as those in S98. From Equation (21) it is clear that the linear polarization of the scattered radiation no longer depends on the strength of the magnetic field.

For an unpolarized beam of light incident on a point source, the fractional polarization (Q/I) resulting from a single scattering (SS) is given by (see Equation (21))

$$\frac{Q}{I} = -\frac{(1-3\mu'^2)(1-\mu^2)}{(8/3 + (1-3\mu^2)(1-3\mu'^2)/3)}. \quad (22)$$

This equation is the same as Equation (12) of House (1972), where the symbols θ and θ' are reversed for the linear polarization angle equal to zero and for the $M1$ transition with $J = 0 \rightarrow 1 \rightarrow 0$ (see Table 1 of House 1972 for details). Equation (22) clearly shows that when $\mu'^2 = 1/3$, i.e., when $\theta' = 54.^{\circ}7$, which is called the Van Vleck angle, the linear polarization of the scattered ray becomes zero and undergoes a sign reversal about this angle. When $\theta' < 54.^{\circ}7$, the linear polarization is normal to the direction of $\boldsymbol{B}$ projected on POS and is parallel to projected $\boldsymbol{B}$ for $\theta' > 54.^{\circ}7$.

4. Spherical Tensor Representation of the Scattering Matrix

The spherical tensor representation introduced in Landi Degl'Innocenti (1984) allows us to develop a more compact mathematical formulation of the problem. In addition, the polarization properties of the emitted radiation are expressed in their simplest form in that basis. Hence in this section we express the Hanle-Zeeman scattering matrix derived in Section 3 in terms of the irreducible spherical tensors introduced in Landi Degl'Innocenti (1984) as well as in terms of the generalized profile function introduced by Landi Degl'Innocenti et al. (1991). The procedure for achieving this is described in Sampoorna et al. (2007, hereafter SNS07). We apply this procedure originally written for $E1$ transitions to the case of $M1$ transitions. Following Landi DeglInnocenti & Landolfi (2004, hereafter LL04), we choose the linear polarization unit vectors as

$$\begin{aligned}
\boldsymbol{e}_{-1}(\boldsymbol{n}) &= \frac{1}{\sqrt{2}}[\boldsymbol{e}_a(\boldsymbol{n}) + \mathrm{i}\boldsymbol{e}_b(\boldsymbol{n})],\\
\boldsymbol{e}_{+1}(\boldsymbol{n}) &= \frac{1}{\sqrt{2}}[-\boldsymbol{e}_a(\boldsymbol{n}) + \mathrm{i}\boldsymbol{e}_b(\boldsymbol{n})],\\
\boldsymbol{e}'_{-1}(\boldsymbol{n}') &= \frac{1}{\sqrt{2}}[\boldsymbol{e}'_a(\boldsymbol{n}') + \mathrm{i}\boldsymbol{e}'_b(\boldsymbol{n}')],\\
\boldsymbol{e}'_{+1}(\boldsymbol{n}') &= \frac{1}{\sqrt{2}}[-\boldsymbol{e}'_a(\boldsymbol{n}') + \mathrm{i}\boldsymbol{e}'_b(\boldsymbol{n}')],
\end{aligned} \tag{23}$$

where $[\boldsymbol{e}_a(\boldsymbol{n}), \boldsymbol{e}_b(\boldsymbol{n}), \boldsymbol{n}]$ form a right-handed coordinate system about the outgoing ray and similarly a primed system for the incoming ray. Here $\boldsymbol{e}_a(\boldsymbol{n})$ and $\boldsymbol{e}_b(\boldsymbol{n})$ represent the linear polarization basis vectors. The relation between radiation electric and magnetic field vectors depends on the choice of linear polarization basis vectors. In the classical derivation for $M1$ transitions presented in Section 3, the linear polarization basis vectors were $\boldsymbol{e}_a(\boldsymbol{n})$ and $\boldsymbol{e}_b(\boldsymbol{n})$ (which are denoted as $\boldsymbol{e}_\alpha$ with $\alpha = 1, 2$ in Section 3 following S98). In this basis the relation between the radiation electric and magnetic field vectors is given by Equation (9). In the present section we use the linear polarization basis vectors defined in Equation (23). To find the relation between the radiation electric and magnetic field vectors in the basis $\boldsymbol{e}_{+1}(\boldsymbol{n})$ and $\boldsymbol{e}_{-1}(\boldsymbol{n})$, we therefore use the relation $E_1\boldsymbol{e}_a + E_2\boldsymbol{e}_b = E_{+1}\boldsymbol{e}_{+1} + E_{-1}\boldsymbol{e}_{-1}$ and $\boldsymbol{E} = \boldsymbol{B} \times \hat{\boldsymbol{r}}$ and find that $\boldsymbol{B} = (\mathrm{i}E_{+1})\boldsymbol{e}_{+1} + (-\mathrm{i}E_{-1})\boldsymbol{e}_{-1}$. Therefore the spherical vector components of the radiation electric and magnetic fields are related through

$$B_\delta = \mathrm{i}\,\delta E_\delta; \quad E_\delta = -\mathrm{i}\,\delta B_\delta, \quad \delta = \pm 1. \tag{24}$$

Similar relations also hold good for the primed system. Following Equations (C1) and (C2) of SNS07, the magnetic field components of the scattered radiation can be written as

$$B^{\mathrm{out}}_\mu \sim \sum_{\rho q} \Phi_q [e_\mu(\boldsymbol{n})]^*_q [e'_\rho(\boldsymbol{n}')]_q B^{\mathrm{in}}_\rho. \tag{25}$$

Using Equation (24), we can rewrite the above equation as

$$E^{\mathrm{out}}_\mu \sim \sum_{\rho q} \mu\rho\Phi_q [e_\mu(\boldsymbol{n})]^*_q [e'_\rho(\boldsymbol{n}')]_q E^{\mathrm{in}}_\rho, \quad \mu, \rho = \pm 1. \tag{26}$$

Following S94, we define the coherency matrix $I^S_{\mu\nu} = E^{\mathrm{out}}_\mu E^{\mathrm{out}*}_\nu$, where the superscript S stands for S94. From Equation (26) we can write $I^S_{\mu\nu}$ for $M1$ transitions

$$I^S_{\mu\nu} = \sum_{\rho\sigma} T^{S,M1}_{\mu\nu,\rho\sigma}(\omega, \boldsymbol{n}, \boldsymbol{n}'; \boldsymbol{B}) I'^S_{\rho\sigma}, \tag{27}$$

where

$$\begin{aligned}
T^{S,M1}_{\mu\nu,\rho\sigma}(\omega, \boldsymbol{n}, \boldsymbol{n}'; \boldsymbol{B}) = \sum_{qq'} \mu\nu\rho\sigma\ \Phi_q\Phi^*_{q'} [e_\mu(\boldsymbol{n})]^*_q\\
\times [e_\nu(\boldsymbol{n})]_{q'} [e'_\rho(\boldsymbol{n}')]_q [e'_\sigma(\boldsymbol{n}')]^*_{q'}.
\end{aligned} \tag{28}$$

Similar to the $E1$ transitions (see LL04), we now define the reducible spherical tensor for the $M1$ transitions as

$$\mathcal{E}^{S,M1}_{qq'}(\mu, \nu, \boldsymbol{n}) = \mu\nu [e_\mu(\boldsymbol{n})]^*_q [e_\nu(\boldsymbol{n})]_{q'}. \tag{29}$$

Therefore Equation (28) can be rewritten as

$$\begin{aligned}
T^{S,M1}_{\mu\nu,\rho\sigma}(\omega, \boldsymbol{n}, \boldsymbol{n}'; \boldsymbol{B}) = \frac{3}{2} \sum_{qq'} \Phi_q\Phi^*_{q'} \mathcal{E}^{S,M1}_{qq'}(\mu, \nu, \boldsymbol{n})\\
\times \mathcal{E}^{S,M1}_{q'q}(\sigma, \rho, \boldsymbol{n}'),
\end{aligned} \tag{30}$$

where the factor $3/2$ is the normalization constant (see S94). We now transform from coherency matrix basis to the Stokes vector basis (see S94 as well as Appendix C of SNS07). Thus the scattered Stokes vector S_i (with $i = 0, 1, 2, 3$) can be written as

$$S_i = \sum_{j=0}^{3} P^{M1}_{ij}(\omega, \boldsymbol{n}, \boldsymbol{n}'; \boldsymbol{B}) S'_j, \tag{31}$$

with S'_j being the incident Stokes vector, and the phase matrix P^{M1}_{ij} for the M1 transitions is given by

$$\begin{aligned}
P^{M1}_{ij}(\omega, \boldsymbol{n}, \boldsymbol{n}'; \boldsymbol{B}) = \frac{3}{4} \sum_{\mu\nu\rho\sigma qq'} \Phi_q\Phi^*_{q'} (\sigma_i)_{\nu\mu} (\sigma_j)_{\rho\sigma}\\
\times \mathcal{E}^{S,M1}_{qq'}(\mu, \nu, \boldsymbol{n}) \mathcal{E}^{S,M1}_{q'q}(\sigma, \rho, \boldsymbol{n}'),
\end{aligned} \tag{32}$$

where σ_i are the Pauli spin matrices. Following LL04, we define

$$\mathcal{T}^{S,M1}_{qq'}(i, \boldsymbol{n}) = \sum_{\mu\nu} \frac{1}{2} (\sigma_i)_{\nu\mu} \mathcal{E}^{S,M1}_{qq'}(\mu, \nu, \boldsymbol{n}). \tag{33}$$

Thus Equation (32) can be rewritten as

$$\begin{aligned}
P^{M1}_{ij}(\omega, \boldsymbol{n}, \boldsymbol{n}'; \boldsymbol{B}) = 3 \sum_{qq'} \Phi_q\Phi^*_{q'} \mathcal{T}^{S,M1}_{qq'}(i, \boldsymbol{n})\\
\times \mathcal{T}^{S,M1}_{q'q}(j, \boldsymbol{n}').
\end{aligned} \tag{34}$$

For mathematical simplicity we express the product of profile functions as proportional to their sums (see S98), namely

$$\Phi_q\Phi^*_{q'} = \frac{1}{2\pi a} \cos\alpha_{q-q'} e^{\mathrm{i}\alpha_{q-q'}} (\Phi_q + \Phi^*_{q'}), \tag{35}$$

where $\alpha_{q-q'}$ is the Hanle angle given by $\tan\alpha_{q-q'} = (q - q')g_b\omega_B/\gamma$, with g_b being the Lande g-factor of the upper level, and $a = \gamma/4\pi\Delta\nu_D$ is the damping parameter with $\Delta\nu_D$ the Doppler width. Following LL04, we introduce the irreducible spherical tensor written in terms of the reducible

spherical tensor:

$$[\mathcal{T}^{K,M1}_{Q}(i,\boldsymbol{n})]^{S} = \sum_{qq'}(-1)^{1+q}\sqrt{3(2K+1)} \times \begin{pmatrix} 1 & 1 & K \\ q & -q' & -Q \end{pmatrix} \mathcal{T}^{S,M1}_{qq'}(i,\boldsymbol{n}), \quad (36)$$

with the inverse relation given by

$$\mathcal{T}^{S,M1}_{qq'}(i,\boldsymbol{n}) = \sum_{KQ}(-1)^{1+q}\sqrt{\frac{(2K+1)}{3}} \times \begin{pmatrix} 1 & 1 & K \\ q & -q' & -Q \end{pmatrix} [\mathcal{T}^{K,M1}_{Q}(i,\boldsymbol{n})]^{S}. \quad (37)$$

Substituting Equations (35) and (37) in Equation (34), we obtain

$$P^{M1}_{ij}(\omega,\boldsymbol{n},\boldsymbol{n}';\boldsymbol{B}) = \sum_{KK'Q}\cos\alpha_{Q}e^{\mathrm{i}\alpha_{Q}}[\mathcal{T}^{K,M1}_{Q}(i,\boldsymbol{n})]^{S} \times [\mathcal{T}^{K',M1}_{-Q}(j,\boldsymbol{n}')]^{S}\Bigg\{\sum_{qq'}(-1)^{q+q'}\sqrt{(2K+1)} \times \sqrt{(2K'+1)}\begin{pmatrix} 1 & 1 & K \\ q & -q' & -Q \end{pmatrix} \times \begin{pmatrix} 1 & 1 & K' \\ q' & -q & Q \end{pmatrix}\frac{1}{2}(\Phi_{q}+\Phi^{*}_{q'})\Bigg\}. \quad (38)$$

We now express the profile function appearing in Equation (38) in terms of the generalized profile function defined in Landi Degl'Innocenti et al. (1991). For the sake of clarity, we recall the definition of the generalized profile function for the $J = 0 \rightarrow 1 \rightarrow 0$ transition:

$$\Phi^{KK'}_{Q}(0,1;\omega) = \sum_{MM'}(-1)^{Q-M-M'} \times \sqrt{(2K+1)(2K'+1)} \times \begin{pmatrix} 1 & 1 & K \\ M' & -M & Q \end{pmatrix}\begin{pmatrix} 1 & 1 & K' \\ -M & M' & Q \end{pmatrix} \times \frac{1}{2}[\phi(\omega_{1M'00}-\omega)+\phi^{*}(\omega_{1M00}-\omega)]. \quad (39)$$

In the above equation the profile function $\phi(\omega_{1M00}-\omega)$ is given by

$$\phi = \frac{-2/\mathrm{i}}{\omega_{0}-\omega+g_{b}M\omega_{B}+\mathrm{i}\gamma/2}. \quad (40)$$

Comparing this equation with Equation (4), we see that $\Phi_{q} = \phi^{*}(\omega_{1-q00}-\omega)$. In Equation (38) we replace $-q$ by M, $-q'$ by M' as well as Q by $-Q$, and using the properties of 3-j symbols, we can identify the resulting term in the flower bracket of Equation (38) to be related to the generalized profile function given in Equation (39). Thus Equation (38) can be rewritten as

$$P^{M1}_{ij}(\omega,\boldsymbol{n},\boldsymbol{n}';\boldsymbol{B}) = \sum_{KK'Q}\cos\alpha_{Q}e^{-\mathrm{i}\alpha_{Q}}(-1)^{Q} \times [\mathcal{T}^{K,M1}_{-Q}(i,\boldsymbol{n})]^{S}[\mathcal{T}^{K',M1}_{Q}(j,\boldsymbol{n}')]^{S}(-1)^{K} \times \Phi^{KK'}_{Q}(0,1;\omega). \quad (41)$$

We now express $[\mathcal{T}^{K,M1}_{Q}]^{S}$ in terms of the irreducible spherical tensors for the $E1$ transitions. The reducible tensor $\mathcal{E}^{S,M1}_{qq'}(\mu,\nu,\boldsymbol{n})$ defined in Equation (29) can be rewritten in terms of the Wigner rotation matrices as

$$\mathcal{E}^{S,M1}_{qq'}(\mu,\nu,\boldsymbol{n}) = \mu\nu\mathcal{D}^{1}_{\mu q}(R)^{*}\mathcal{D}^{1}_{\nu q'}(R), \quad (42)$$

where $R \equiv (0,-\theta,-\phi)$ is a rotation that brings the system $[\boldsymbol{e}_{a}(\boldsymbol{n}),\boldsymbol{e}_{b}(\boldsymbol{n}),\boldsymbol{n}]$ into the system, where the magnetic field is along the polar Z-axis. Substituting for $\mathcal{E}^{S,M1}_{qq'}$ in Equation (33) and the resulting expression for $\mathcal{T}^{S,M1}_{qq'}$ in Equation (36), we obtain

$$[\mathcal{T}^{K,M1}_{Q}(i,\boldsymbol{n})]^{S} = (-1)^{Q}\sum_{Q'}[t^{K,M1}_{Q'}(i)]^{S}\mathcal{D}^{K}_{Q'-Q}(R), \quad (43)$$

where

$$[t^{K,M1}_{Q'}(i)]^{S} = \sum_{\mu\nu}\frac{1}{2}\mu\nu(\sigma_{i})_{\mu\nu}\sqrt{3(2K+1)} \times \begin{pmatrix} 1 & 1 & K \\ \mu & -\nu & -Q' \end{pmatrix}. \quad (44)$$

Defining the quantity

$$\zeta_{i} = (1,-1,-1,1),\ i = 0,1,2,3, \quad (45)$$

corresponding to the Stokes parameters, Equation (44) can be rewritten as

$$[t^{K,M1}_{Q'}(i)]^{S} = \zeta_{i}\sum_{\mu\nu}\frac{1}{2}(\sigma_{i})_{\mu\nu}\sqrt{3(2K+1)} \times \begin{pmatrix} 1 & 1 & K \\ \mu & -\nu & -Q' \end{pmatrix}. \quad (46)$$

Comparing this expression with Equation (C21) of SNS07 (which is for electric dipole transitions), we can write

$$[t^{K,M1}_{Q'}(i)]^{S} = \zeta_{i}[t^{K}_{Q'}(i)]^{S}. \quad (47)$$

With the above expression and Equation (C22) of SNS07, Equation (43) can be rewritten as

$$[\mathcal{T}^{K,M1}_{Q}(i,\boldsymbol{n})]^{S} = \zeta_{i}[\mathcal{T}^{K*}_{Q}(i,\boldsymbol{n})]^{L}, \quad (48)$$

where the superscript "L" stands for LL04. From the above equation it is clear that the irreducible spherical tensor for the $M1$ transition is related to that for the $E1$ transition by the factor ζ_{i} (see also Equation (13.25) of LL04). In terms of irreducible spherical tensor representation of LL04, Equation (41)

therefore becomes

$$P_{ij}^{M1}(\omega, \boldsymbol{n}, \boldsymbol{n}'; \boldsymbol{B}) = \zeta_i \zeta_j \Bigg[\sum_{KK'Q} \cos\alpha_Q e^{-i\alpha_Q} (-1)^Q \mathcal{T}_Q^K(i, \boldsymbol{n}) \mathcal{T}_{-Q}^{K'}(j, \boldsymbol{n}') (-1)^K \Phi_Q^{KK'}(0, 1; \omega) \Bigg], \quad (49)$$

where we have dropped the superscript L without loss of generality. The above equation represents the Hanle-Zeeman scattering matrix for the $M1$ transitions. The term in the square brackets in Equation (49) is identical to the right-hand side of Equation (52) in Bommier (1997), when in the latter the collisions are ignored and only frequency coherent scattering is considered. Therefore the term in the square brackets represents the Hanle-Zeeman scattering matrix for $E1$ transitions. Thus we can write

$$P_{ij}^{M1}(\omega, \boldsymbol{n}, \boldsymbol{n}'; \boldsymbol{B}) = \zeta_i \zeta_j \, P_{ij}^{E1}(\omega, \boldsymbol{n}, \boldsymbol{n}'; \boldsymbol{B}). \quad (50)$$

The above relation between the phase matrices for $M1$ and $E1$ transitions is quite general. Indeed, they differ only through signs of certain matrix elements. The sign differences occur because the driving force for $E1$ and $M1$ transitions are the radiation electric and magnetic fields, respectively, which are independent of the J quantum numbers of the transition involved. Therefore Equation (50) can be used for an arbitrary $J_l \rightarrow J_u \rightarrow J_l$ scattering transition. The corresponding phase matrix P^{E1} can be derived using the Kramers-Heisenberg approach of S98 (see also LL04).

For our further discussions we would like to introduce the non-dimensional frequency in the laboratory frame, which is defined as

$$x = \frac{\omega_0 - \omega}{\Delta\omega_D}, \quad (51)$$

where $\Delta\omega_D = 2\pi\Delta\nu_D$. To account for thermal motion of radiating atoms, the profile function in the rest frame $\phi(\omega_{1M00} - \omega)$ is convolved with the Maxwellian velocity distribution. Thus the laboratory frame profile function is given by

$$\mathcal{H}(a, x_M) = H(a, x_M) + i\, F(a, x_M), \quad (52)$$

where $H(a, x_M)$ is the normalized Voigt function describing absorption and $F(a, x_M)$ is the normalized Faraday-Voigt function describing dispersion with $x_M = x + g_b M\nu_B/\Delta\nu_D$ (see Section 2.3 of S98 for details).

Equation (50) shows that the scattering matrix derived for $M1$ transition is related to that of $E1$ transition in a simple manner. To illustrate this, we consider an SS of an unpolarized beam of radiation incident on the scattering atom in the vertical direction. The Stokes parameters of the scattered radiation are then given by the first column of the phase matrix. Figure 4 shows the polarization diagram, namely the plot of U/I versus Q/I for $x = 0$ as a function of field strength parameter $\Gamma_B = g_b\omega_B/\gamma$ for different choices of magnetic azimuthal angles φ_B and a fixed field inclination angle $\vartheta_B = \pi/2$ (see Figure 3). From Equation (50), we see that Q/I and U/I for $M1$ transitions differ from those for $E1$ transitions by a negative sign. This is clearly reflected in Figure 4. For example, note that Q/I values are negative for $E1$ transitions, while they are positive for $M1$ transitions. As for U/I, let us take the example of $\varphi_B = 0°$. It is negative for all values of Γ_B in $E1$ transitions, while it is positive for M1 transitions. As expected, the magnitudes remain the same. The symmetry properties of the polarization diagram with respect to $\varphi_B = \pm\pi/2$, $\pm\pi/4$ and $\pm 3\pi/4$ are identical for both $E1$ and $M1$ transitions. Furthermore, for a given ϑ_B and φ_B, the U/I initially increases, reaches a maximum for $\Gamma_B = 0.5$, and then decreases and saturates for $\Gamma_B \gg 1$.

5. Integration over the Solid Angle of the Incident Cone of Radiation

For mathematical simplicity the phase matrix for $M1$ transitions was derived in the previous sections in the MRF (with the Z-axis along the magnetic field direction). For practical purposes we need the scattering matrix in a more general geometry, called the atmospheric reference frame (ARF, see Figure 3). Following LL04 (see also Frisch 2007), Equation (49) can now be written in ARF as

$$P_{ij}^{M1}(x, \boldsymbol{n}, \boldsymbol{n}'; \boldsymbol{B}) = \zeta_i \zeta_j \Bigg[\sum_{KQ} (-1)^K \mathcal{T}_Q^K(i, \boldsymbol{n}) \times \sum_{K'Q'} N_{QQ'}^{KK'}(x, \boldsymbol{B}) (-1)^{Q'} \mathcal{T}_{-Q'}^{K'}(j, \boldsymbol{n}') \Bigg]. \quad (53)$$

Here, $\boldsymbol{n}$ and $\boldsymbol{n}'$ are now defined by their polar angles ϑ, φ and ϑ', φ' in the ARF. The magnetic kernel $N_{QQ'}^{KK'}(x, \boldsymbol{B})$ may be written as

$$N_{QQ'}^{KK'}(x, \boldsymbol{B}) = e^{i(Q'-Q)\varphi_B} \sum_{Q''} d_{QQ''}^K(\vartheta_B) \times d_{Q''Q'}^{K'}(-\vartheta_B) \cos\alpha_{Q''} e^{-i\alpha_{Q''}} \Phi_{Q''}^{KK'}(0, 1; x), \quad (54)$$

where ϑ_B and φ_B are the polar angles of the magnetic field in ARF. Expressions for the reduced rotation matrices $d_{QQ'}^K$ can be found in LL04 (see their Table 2.1).

The scattering atom in the corona is illuminated by the unpolarized cone of radiation incident from the photosphere (see Figure 1). Thus the scattering matrix has to be integrated over the solid angle subtended by this cone at the sight of the atom. The resulting scattered Stokes parameters are given by

$$\mathcal{I}_i^{M1}(x, \vartheta, \varphi; \boldsymbol{B}) = \int_0^{2\pi} \int_{\cos\Omega}^1 P_{i0}^{M1}(x, \boldsymbol{n}, \boldsymbol{n}'; \boldsymbol{B}) \times I' \frac{d\mu' d\varphi'}{4\pi}, \quad (55)$$

where $\mu' = \cos\vartheta'$. To perform the above integration, we consider a limb-darkening function to represent the angular distribution of incident radiation I' within the cone. This is given by

$$I' = I_o \left[1 - u + \frac{\sqrt{\cos^2\vartheta' - \cos^2\Omega}}{\sin\Omega} \right], \quad (56)$$

where u is an empirically determined limb-darkening coefficient and the solid angle Ω is defined as $\sin\Omega = R_\odot/(R_\odot + h)$, with h being the height of the scattering atom above the photosphere.

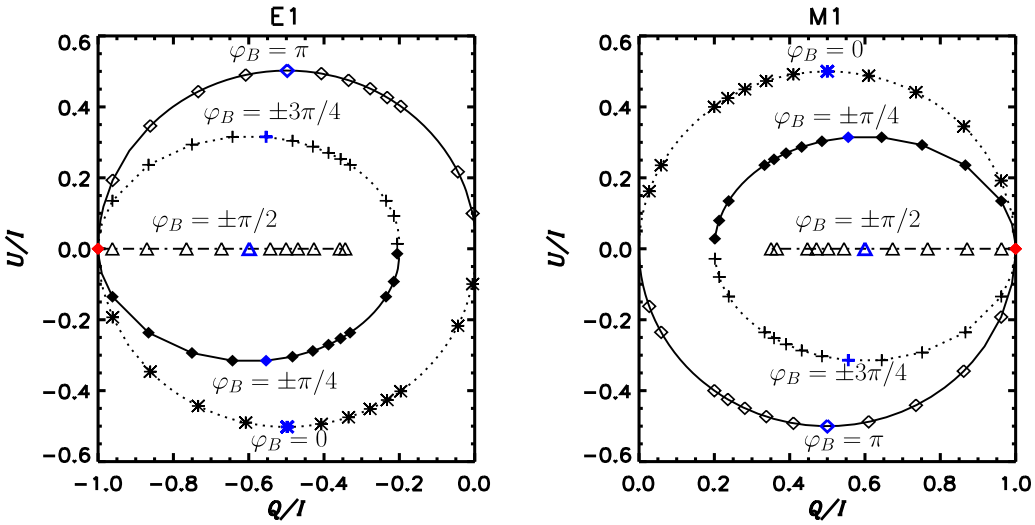

Figure 4. Polarization diagram for $E1$ (left) and $M1$ (right) $J = 0 \rightarrow 1 \rightarrow 0$ transitions. Fractional polarizations Q/I and U/I are plotted as a function of field-strength parameter Γ_B for various values of the magnetic field azimuth angle φ_B and a fixed inclination angle $\vartheta_B = \pi/2$. An unpolarized radiation beam is incident on the atom in the vertical direction ($\vartheta' = 0°$ and $\varphi' = 0°$). The scattered Stokes parameters are calculated in the horizontal plane ($\vartheta = 90°$ and $\varphi = 0°$). The symbols along the different curves correspond to different values of Γ_B (increasing from left to right for $E1$ transitions and from right to left for the $M1$ transitions). $\Gamma_B = 0$ is marked by the filled red symbol. The blue symbols correspond to $\Gamma_B = 0.5$.

Following Frisch (2007), we write the irreducible spherical tensors

$$\mathcal{T}^K_Q(i, \boldsymbol{n}) = \tilde{\mathcal{T}}^K_Q(i, \vartheta) e^{iQ\varphi}. \tag{57}$$

Introducing Equation (57) in Equation (53) and the resulting expression in Equation (55), we see that the integration over φ' will be non-zero only for $Q' = 0$. Now expanding the summation over K', Equation (55) can be written as

$$\mathcal{I}^{M1}_i(x, \vartheta, \varphi; \boldsymbol{B}) = \frac{\zeta_i}{2} \sum_{KQ} (-1)^K \mathcal{T}^K_Q(i, \boldsymbol{n}) \times \left[N^{K0}_{Q0} \int_{\cos\Omega}^{1} \tilde{\mathcal{T}}^0_0(0, \vartheta')\, I'\, d\mu' + N^{K2}_{Q0} \int_{\cos\Omega}^{1} \tilde{\mathcal{T}}^2_0(0, \vartheta') I'\, d\mu' \right]. \tag{58}$$

After introducing the values for $\tilde{\mathcal{T}}^0_0(0, \vartheta')$ and $\tilde{\mathcal{T}}^2_0(0, \vartheta')$ from LL04 (Table 5.6, with a particular choice of the reference angle $\gamma = 0$), the two integrations appearing in Equation (58) can be performed analytically and the resulting expressions are given by

$$\int_{\cos\Omega}^{1} \tilde{\mathcal{T}}^0_0(0, \vartheta')\, I\, d\mu' = (1 - u)(1 - \cos\Omega) + \frac{u}{2}[1 - \cot\Omega \cos\Omega \ln(\sec\Omega + \tan\Omega)],$$

$$\int_{\cos\Omega}^{1} \tilde{\mathcal{T}}^2_0(0, \vartheta') I\, d\mu' = \frac{1}{2\sqrt{2}} \Bigg\{ (1 - u)\cos\Omega \sin^2\Omega + 3u \left[\frac{1}{4} - \frac{1}{8}\cos^2\Omega - \frac{1}{8}\cot\Omega\cos^3\Omega \ln(\sec\Omega + \tan\Omega) \right] - \frac{u}{2}[1 - \cos\Omega\cot\Omega \ln(\sec\Omega + \tan\Omega)] \Bigg\}. \tag{59}$$

From here on, for all the illustrations presented in this paper, we consider scattering on the [Fe XIII] ion located at a height $h = 0.5\, R_\odot$ above the limb. In particular, we consider the 10747 Å line that results from $^3P_0 \rightarrow {}^3P_1 \rightarrow {}^3P_0$ scattering transition. We chose this line because it is expected to be used for the spectropolarimetric studies of the solar corona by the Visible Emission Line Coronagraph (VELC) payload on board Aditya-L1[4], an upcoming Indian space mission to study the Sun. VELC is designed to image the solar corona over a field of view (FOV) of 1.05 $R_\odot$ to 3 $R_\odot$ and further facilitates spectropolarimetric studies of the 10747 Å line over a FOV of 1.05 $R_\odot$ to 1.5 $R_\odot$.

We use two-level atom approximation and neglect collisions. The effects of collisions and multilevel coupling are discussed in detail in House (1977) and Sahal-Bréchot (1977). These authors show that the two-level atom approximation is insufficient particularly when electron densities are higher than 10^7 cm^{-3}. This is because in such cases the collisional effects cannot be neglected. Indeed, the ground configuration of the [Fe XIII] ion consists of five levels, namely, $^3P_0$, $^3P_1$, $^3P_2$, $^1D_2$, and $^1S_0$. Sahal-Bréchot (1977) has demonstrated that the collisional transfer from the $^3P_2$ level (and also other higher levels) plays an important depolarizing role. In particular, the collision effects decrease the degree of linear polarization of the [Fe XIII] 10747 Å line by about 10% (see also Figure 4(d) of House 1977). Therefore the theoretical formalism presented in this paper can be applied to only those regions in the corona where the electron densities are lower than 10^7 cm^{-3}. For the electron density model considered by House (1977, see his Table 2 and see also Equation (62) below), such densities are found for $h \gtrsim 0.5\, R_\odot$ above the limb. We present all the results for $h = 0.5\, R_\odot$ (which is the upper limit for spectropolarimetric observations of the Aditya-L1 mission). For $h < 0.5\, R_\odot$ it is essential to account for the collisional effects and thereby the multilevel coupling.

Although we use a two-level atom approximation and neglect collisions, our theoretical formalism is able to handle a wide range of field strengths, unlike previous formalisms

[4] http://www.isro.gov.in/aditya-l1-first-indian-mission-to-study-Sun (2016 May 12th).

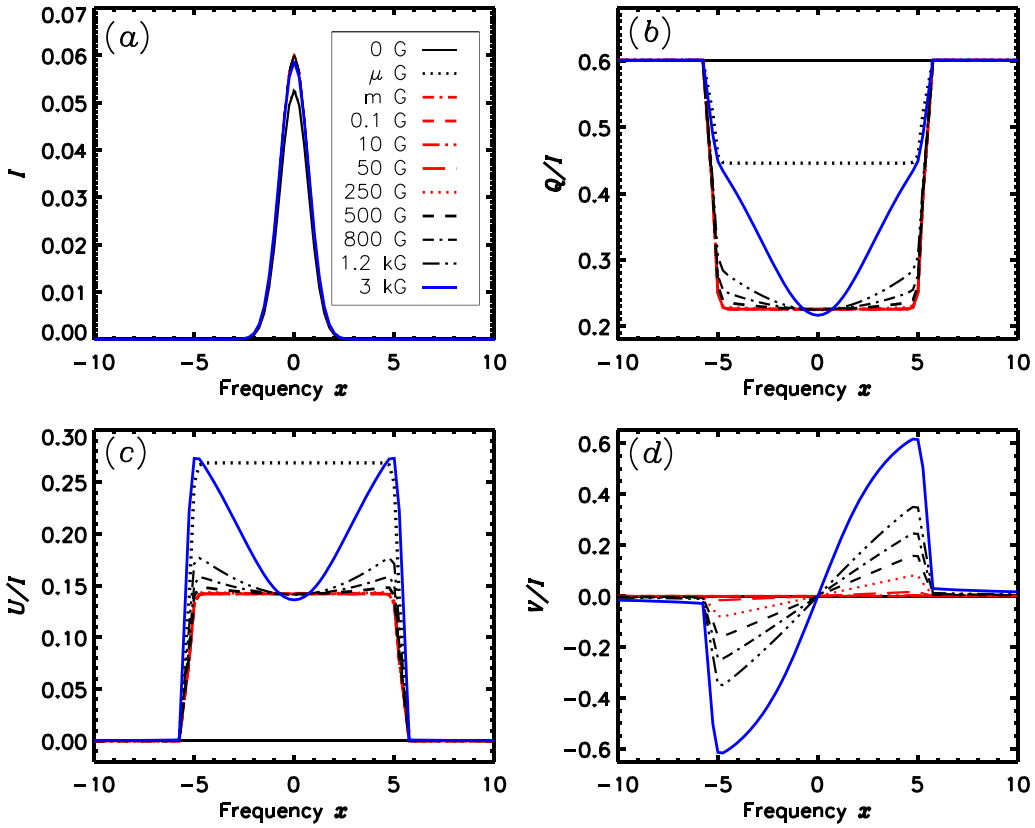

Figure 5. Scattered Stokes profiles from a height of 0.5 $R_\odot$ above the limb after the integration over the incident cone of radiation from the photosphere. The model parameters are (A, ϑ, φ, ϑ_B, φ_B, $\Delta\lambda_D$, u) = (14.04 s^{-1}, 90°, 90°, 30°, 60°, 0.87 Å, 0.34).

(House 1977; Sahal-Bréchot 1977; Casini & Judge 1999), which only considered the saturated Hanle regime. For our illustrations we therefore consider a range of field strengths from μG to 3 kG. However, the coronal magnetic fields are expected to fall in the range 1–30 G (Lin et al. 2000; Jess et al. 2016), which corresponds to the saturated Hanle regime for the [Fe XIII] 10747 Å line. In spite of this, we consider field strengths outside this range to demonstrate the applicability of our approach to arbitrary-strength fields. In the stellar case, the 10747 Å line has been observed by Zirin (1976) in R Aquarii, which is a symbiotic star. Extremely weak fields on the order of μG are expected to be found in diffuse media such as the interstellar medium (ISM), circumstellar regions, supernova remnants, etc. (see, e.g., Yan & Lazarian 2006; Ferriére 2009; Reynolds et al. 2012). In such diffuse media, several forbidden lines of [O I], [O III], [Ne II], [Ne V], [Ca II], [S II], [Fe II], [Fe XIV], and [Fe X] (Kraus et al. 2010; Dopita et al. 2016) are formed. Indeed, the IR forbidden lines of neon are formed in the winds of Wolf-Rayet stars (Ignace & Brimeyer 2006), where fields as strong as 1.5 kG are expected (de la Chevrotiére et al. 2014). More recently, the polarization of [O I] 6300 Å line formed in the solar photosphere has been observed (de Wijn et al. 2017). Our theoretical formalism can be applied to compute the linear polarization profiles of any $M1$ forbidden line (see the text below Equation (50)) in the presence of arbitrary-strength magnetic fields (that are found in the ISM, stellar winds, and also in solar and stellar atmospheres), provided the collisions and multilevel couplings are negligible.

Figure 5 shows the scattered Stokes profiles obtained after integrating over a cone of radiation incident from the photosphere (see Equations (58) and (59)). The limb-darkening coefficient $u = 0.34$ is used (see Pierce 2000). The field strength is varied in a wide range from μ G to 3 kG. Because the Einstein A coefficient for the chosen transition is very small (about 14.04 s^{-1}), the field strength parameter Γ_B is very large, so that the profiles remain in the saturated Hanle regime for a wide range of field strengths (shown as red curves covering the range from mG to 250 G). At a coronal temperature of 2 MK, the Doppler width is large (about 0.87 Å), therefore the intensity profiles become insensitive to the field strength variation. As the field strength increases, the Q/I profiles become depolarized in the line core and reach a saturated value (with no variation with field strength up to 250 G). Similar to Q/I, the U/I first increases (for μ G field) and then decreases (for mG field) and remains in the saturated regime up to 250 G. For fields larger than 250 G, the Q/I and U/I profiles exhibit typical Zeeman-like behavior. The V/I profiles exhibit a typical antisymmetric shape with increasing amplitudes as a function of field strength.

6. Line-of-sight (LOS) Integration

The polarization of the coronal emission lines measured by an observer at Earth is influenced by the density variation of the scattering ions along the LOS. As the corona is optically thin, it is sufficient to integrate the scattering contributions from atoms along the LOS. The geometry chosen for the LOS integration is shown in Figure 6. In this geometry the primed coordinate system $x'y'z'$ is fixed to the Sun with the $x'z'$ plane describing the POS and y' axis is chosen along the LOS. The unprimed coordinate system xyz is oriented at an angle χ with respect to the $x'y'z'$ system with x' parallel to x. This xyz system describes the ARF where the atom is considered to be

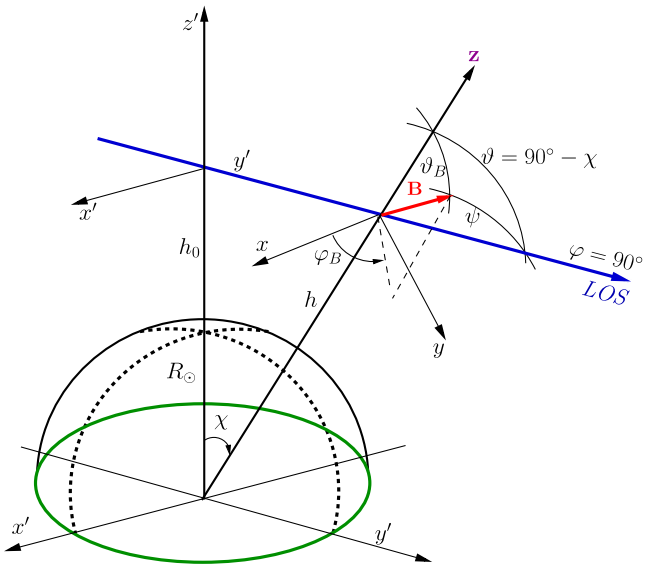

Figure 6. Geometry used for integration along the LOS (see the text for details).

fixed at its origin at a height h above the limb. The LOS makes an angle $\vartheta = 90° - \chi$ with respect to the z-axis and has an azimuth $\varphi = 90°$. ψ is the angle between $\boldsymbol{B}$ and LOS. The distance along the LOS as measured from the mid-plane ($\chi = 0$) in units of $R_\odot$ is given by

$$l = (1 + \rho_0)\tan\chi, \tag{60}$$

where $\rho_0 = h_0/R_\odot$. The solid angle subtended by the cone of incident radiation at the scattering point can now be defined as $\sin\Omega = 1/(1 + \rho)$, where $\rho = h/R_\odot$. This can also be written in terms of χ using $\cos\chi = (1 + \rho_0)/(1 + \rho)$, which then gives $\sin\Omega = \cos\chi/(1 + \rho_0)$. The integration along the LOS can now be expressed in the following form:

$$I_i^{M1}(x, \rho_0) = \int_{-\pi/2}^{\pi/2} \mathcal{I}_i^{M1}(x, \vartheta, \varphi; \boldsymbol{B}) N(\rho, \chi) \times \frac{(1 + \rho_0)}{\cos^2\chi}\, d\chi, \tag{61}$$

where $N(\rho, \chi)$ is the relative density distributions of the scattering ions along the LOS.

The LOS integral in Equation (61) is performed numerically using Simpson's 1/6th integration formula along with equally spaced points in the χ-grid. We find that 11 points χ-grid is sufficient to accurately evaluate the LOS integral. For the purpose of comparison, we have used all the five different density variations that are listed as Cases 1–5 in House (1972). We find that the variation of degree of linear polarization with height above the limb for all the five cases given in Tables 2 and 3 of House (1972) can be reproduced with an accuracy of 2%–8% for the limb-darkening coefficient value $u = 1$ and for a $J = 0 \rightarrow 1 \rightarrow 0$ scattering transition. For illustration, in Figure 7 we plot the frequency-integrated degree of linear polarization as a function of height above the limb for the density distribution in Case 5 of House (1972) given by $N \propto k_4 \exp(-\beta_4 \rho)$ with $k_4 = 1$, $\beta_4 = 0$ and for a radial field. The small differences between the P max computed by House (1972) and our computations could be due to different methods of integration.

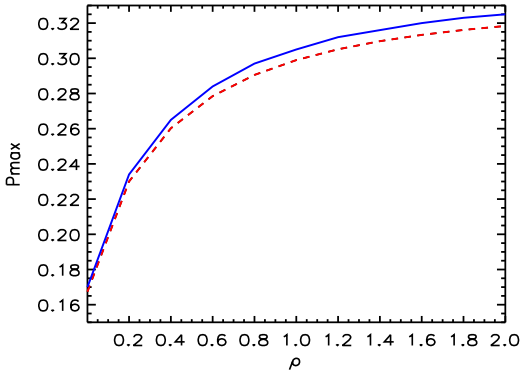

Figure 7. Degree of linear polarization (P max $= \sqrt{(Q^2 + U^2)}/I$) as a function of height above the limb in $R_\odot$ units for density distribution in Case 5 of House (1972) for $u = 1$. The blue solid line corresponds to the data given in Table 3 of House (1972) and the red dashed line corresponds to P max computed by us.

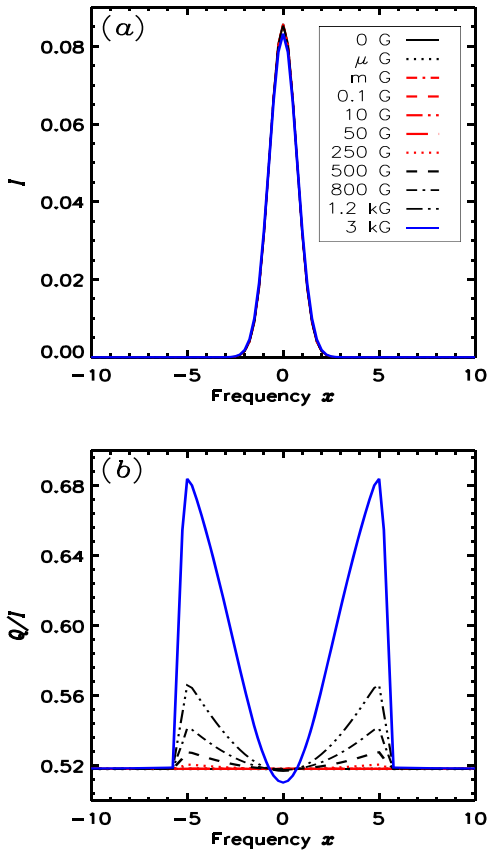

Figure 8. LOS-integrated Stokes profiles at $h = 0.5\ R_\odot$ for the radial field. The model parameters are (A, ϑ_B, φ_B, $\Delta\lambda_D$, u) = (14.04 s^{-1}, 0°, 0°, 0.87 Å, 0.34). The density distribution is given by Equation (62).

For further studies presented in this paper we adopt the spherically symmetric density distribution model used in House (1972), which is given by

$$N = \sum_{i=1}^{3} k_i (1 + \rho)^{-\beta_i}, \tag{62}$$

where $k_1 = 7.55$, $k_2 = -1.68$, $k_3 = 1.04 \times 10^3$, $\beta_1 = 5.35$, $\beta_2 = 14.74$, and $\beta_3 = -20.45$. These values are taken from Newkirk et al. (1970).

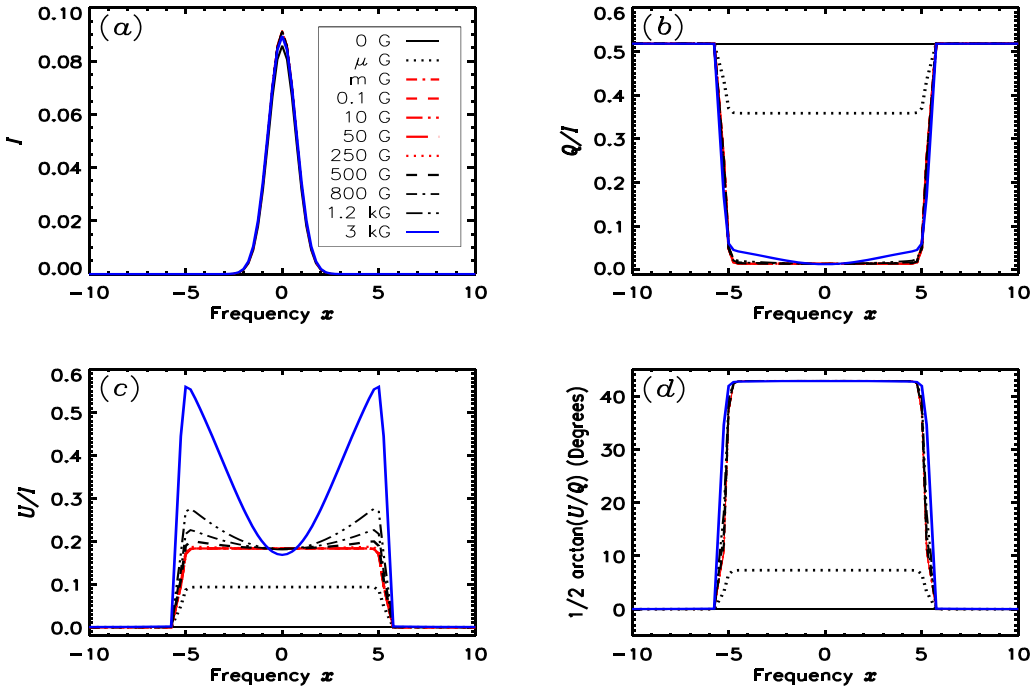

Figure 9. LOS-integrated Stokes profiles (panels a, b, c) and the position angle $= 1/2 \arctan(U/Q)$ as a function of frequency for the dipole field with a colatitude of 60°. The LOS is at a height of 0.5 $R_\odot$ above the limb. The model parameters are (A, ϑ_B, φ_B, $\Delta\lambda_D$, u) = (14.04 s^{-1}, 40°89, 0°, 0.87 Å, 0.34). The density distribution is given by Equation (62). The dipole axis is in the POS, which makes an angle of 90° with respect to the LOS.

6.1. Radial and Dipole Magnetic Field Configurations

Using the density distribution given in Equation (62), we compute the LOS-integrated Stokes profiles for the radial field ($\vartheta_B = 0°$ and $\varphi_B = 0°$, see Figure 8) and also for the dipole field (see Figure 9) with a fixed colatitude of 60° at all the spatial points along the LOS. For simplicity we consider the case where the dipole field axis and the stellar rotation axis are aligned and remain vertical in the POS. The field strength is varied as discussed in Section 5. The limb-darkening coefficient is fixed at 0.34.

For a radial field, the magnetic field is along the radius vector at each spatial point along the LOS. Thus the azimuthal symmetry of the problem is retained. In this case, Q/I remains at the non-magnetic (Rayleigh) scattering value throughout the line profile for fields of up to 250 G (see Figure 8) and the U/I is zero. This can be understood using Equations (54) and (58). From Equation (54) we see that for radial field ($\vartheta_B = 0°$ and $\varphi_B = 0°$), $N^{KK'}_{QQ'}$ is non-zero only for $Q = Q' = 0$ and depends on the magnetic field strength only through the generalized profile function (and not through the Hanle angles as $Q'' = 0$). For fields weaker than 250 G, the profile functions correspond to different Zeeman components $\mathcal{H}(a, x_{\pm 1}) \approx \mathcal{H}(a, x_0)$. Therefore $N^{KK'}_{00}(x, \boldsymbol{B})$ is nearly equal to the corresponding Rayleigh value. Furthermore, in Equation (58) $\mathcal{T}^K_0(i, \boldsymbol{n})$ alone contributes to the radial field case. For our choice of reference angle $\gamma = 0$, $\mathcal{T}^2_0(2, \boldsymbol{n})$ is zero (see Table 5.6 of LL04), thereby giving rise to $U = 0$ for the radial field case. For fields beyond 250 G, we enter the Zeeman regime, resulting in Zeeman-like Q/I profiles. U/I profiles are zero due to the reasons explained above. The LOS-integrated V/I profile is zero for radial field due to exact cancellation of the V/I in the forward part of the hemisphere ($\chi > 0°$) by the V/I formed at the corresponding spatial points in the backward part of the hemisphere ($\chi < 0°$). This is due to the opposite signs of the longitudinal component of the radial magnetic field in the forward and backward parts of the hemisphere.

For a dipole field, the azimuthal symmetry is broken, because of which both Q/I and U/I are non-zero. For very weak fields (μG) typical Hanle-like signatures are obtained (see black dotted line in Figure 9), which then saturate for mG to 250 G fields. Again, Zeeman signatures are observed for fields stronger than 250 G. Like in the case of radial field, the LOS-integrated V/I is zero because the values of V/I at the χ-grid points along the LOS are perfectly antisymmetric about the mid-plane ($\chi = 0°$, see Figure 10). Figure 9(d) shows the position angle plotted as a function of frequency. It can be clearly observed that the position angle remains constant within the line core at 43° in the saturated Hanle regime. In the line wings the position angle is zero because of the Rayleigh scattering at those frequencies. To study the variation of profiles along the grid points along the LOS, we plot the profiles as a function of angle χ (see Figure 10). We have plotted this for the dipole field case. It shows that the curves are symmetric about $\chi = 0°$, i.e., when the direction of the field is in the POS.

Figure 11 shows a plot of a frequency-integrated degree of polarization $P\,\mathrm{max} = \sqrt{Q^2 + U^2}/I$ as a function of height above the limb. To illustrate the effect of LOS integration, we plot P max computed with (blue lines) and without (red lines) LOS integration. We consider three different cases, namely, (a) a magnetic field with $\vartheta_B = 30°$ and $\varphi_B = 60°$, (b) a radial field, and (c) a dipole field with a colatitude of 60°. When LOS integration is neglected, the P max represents the emission from a given point in the corona. The effect of LOS integration starts to show up for $\rho > 0.4$. The LOS integration results in a

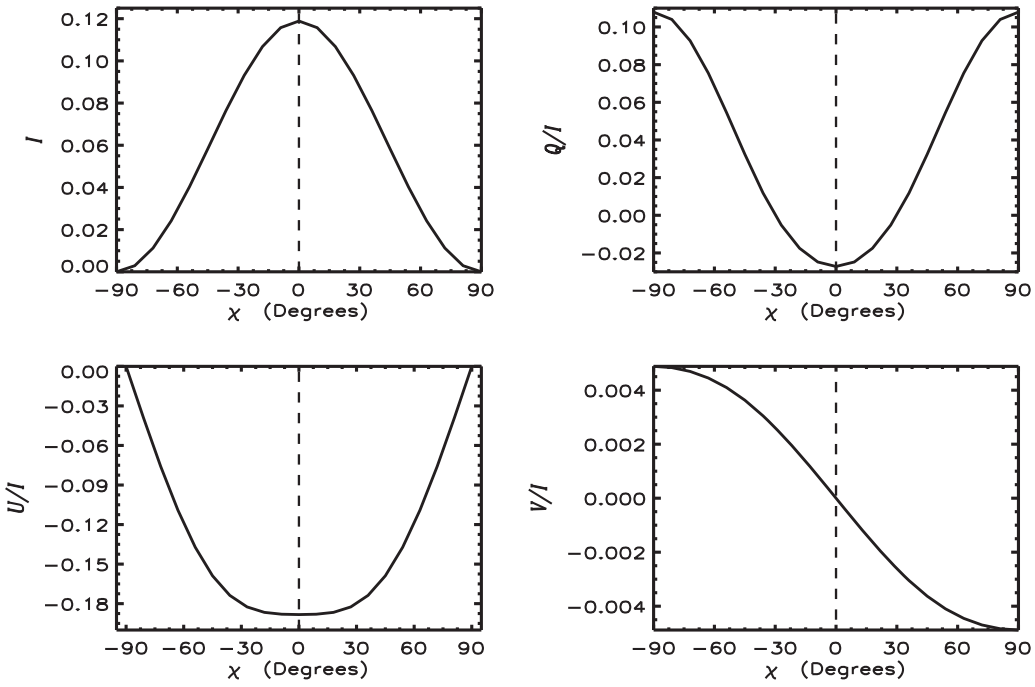

Figure 10. Variation of I, Q/I, and U/I at line center ($x = 0$) and V/I at the frequency corresponding to its peak value at different spatial points (represented by different values of χ) along the LOS. A dipole field with a colatitude of 60° is considered. Note that I, Q/I, and U/I are symmetric about $\chi = 0°$, while V/I is antisymmetric. A constant field strength of $B = 10$ G is used.

decrease of P max because of a mixing of (Q/I, U/I) contributions from various spatial points along the LOS. In Figure 11(d) we plot LOS-integrated log(I) as a function of height for the dipole field case. We clearly see the sharp decrease of intensity with height. This decrease in brightness across the disk basically represents the center-to-limb variation in the corona.

6.2. Symmetry Properties of M1 Scattering Matrix

We study the symmetry properties of $M1$ scattering matrix by considering the variation of the magnetic field orientation on the POS. Figure 12 shows the polarization diagram as a function of field azimuth φ_B, which is varied in the full range 0° to 360° for different field inclination ϑ_B. We consider ϑ_B in the range [0°, 90°] in steps of 10°. The LOS-integrated U/I and Q/I at $x = 0$ are plotted. For $\vartheta_B = 0°$, from Equations (54) and (58) we obtain $U/I = 0$ and Q/I takes the Rayleigh scattered value (φ_B independent). Thus this case represents a point (denoted by plus symbol) in the polarization diagram. For $\vartheta_B \neq 0°$, the breaking of the azimuthal symmetry results in open solid curves in the polarization diagram. As ϑ_B increases, the curvature of these open solid curves increases. The curves are open because we are in the regime of the saturated Hanle effect. The size of the curves initially increases with ϑ_B and decreases as ϑ_B approaches the Van Vleck angle (54.°7). For ϑ_B larger than the Van Vleck angle, (Q/I, U/I) change their sign and the sense of variation with φ_B is reversed (shown by the green solid lines in Figure 12). Furthermore, the size of the polarization diagram also increases. Finally, for $\vartheta_B = 90°$ the polarization diagram becomes a straight line ($U/I = 0$) with a periodicity of $\varphi_B = 90°$ with respect to the φ_B variation.

The polarization diagrams overlap for (ϑ_B, φ_B) and ($180° - \vartheta_B$, $-\varphi_B$). This symmetry property is observed in both the Hanle regime (figure not shown) and in the saturated Hanle regime. In the latter regime, an additional symmetry is seen with respect to φ_B, namely, for any ϑ_B the polarization diagrams overlap for φ_B and $180° - \varphi_B$. These symmetry properties result in the ambiguity in the pair of Stokes parameters (Q/I, U/I), namely, the same values of (Q/I, U/I) are obtained for four different choices of the field orientations mentioned above. These are the traditional 180° ambiguities arising due to the symmetry properties of the scattering matrix. In addition to these ambiguities, there is another source of ambiguity in the Stokes parameters that formed in the saturated Hanle regime. This is the so-called Van Vleck ambiguity that was originally noted by House (1977, see also Casini & Judge 1999), which occurs in a narrow angular range of field orientations around the Van Vleck angle (54.°7). For example, the curves for $\vartheta_B = 40°$ and $\vartheta_B = 80°$ in the polarization diagram (Figure 12) intersect at two points that are marked as red dots. This ambiguity adds to the traditional ambiguity discussed above. Thus there could be six pairs of (ϑ_B, φ_B) values that produce the same values of (Q/I, U/I).

Figure 13 shows the polarization diagram for a very weak field of 1 μG (panel a) in the Hanle regime and for 10 G (panel b) in the saturated Hanle regime. The field inclination is fixed at $\vartheta_B = 30°$ and φ_B is varied from 0° to 360°. In the Hanle regime the polarization diagram executes Lissajous figures (namely, closed loops), in comparison to open curves in saturated Hanle regime. In Figure 13 we present the polarization diagrams computed using (i) pure SS of an incident vertical beam of radiation in the mid-plane (dashed curves), (ii) after integrating over a cone of incident photospheric radiation (also called disk integrated in the literature—DI) at a height of $h = 0.5\ R_\odot$ (dot-dashed curves), and (iii) the same as case (ii), but performing an integration along the LOS (dash-triple-dotted curves). The size of the polarization diagram decreases from case (i) to case (iii). This is expected as the SS represents a case

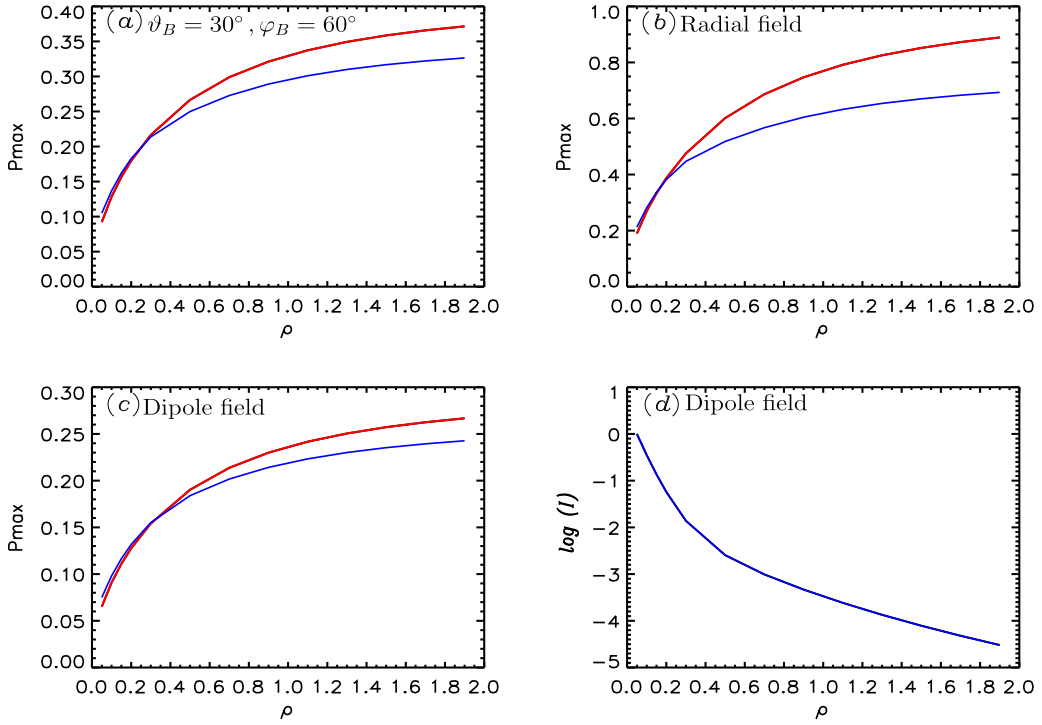

Figure 11. Frequency-integrated degree of linear polarization *P*max ($\sqrt{(Q^2 + U^2)}/I$ (panels a–c) and log(*I*) (panel d) as a function of height above the limb. *P*max computed with (blue line) and without (red line) LOS integration are shown. For all the points a constant field strength of $B = 10$ G is used.

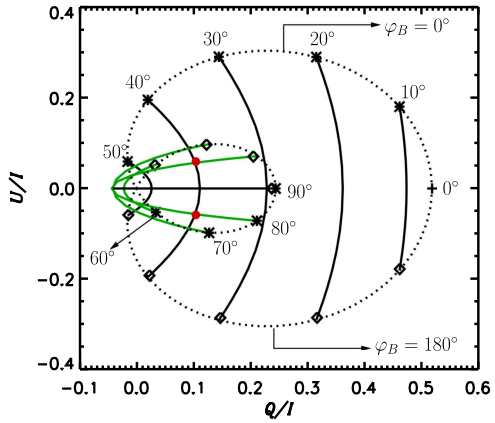

Figure 12. Polarization diagram for varying $\vartheta_B \in [0°, 90°]$ and $\varphi_B \in [0°, 360°]$ for a constant field strength $B = 10$ G. The LOS is at $h = 0.5\ R_\odot$. The case of $\vartheta_B = 0°$ is represented by the plus, and the following curves correspond to different values of ϑ_B increasing in steps of 10°. The points corresponding to $\varphi_B = 0°$ and 360° are marked by an asterisk, and $\varphi_B = 180°$ are marked by diamonds. As φ_B increases from 0° to 180° in steps of 10°, we move along the curve from asterisk to diamond. For φ_B between 180° and 360°, the curve is retraced from diamond to asterisk.

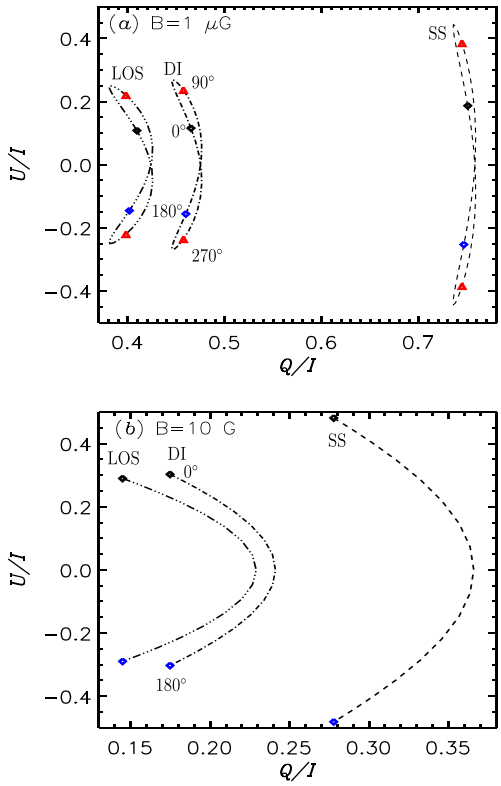

Figure 13. Polarization diagram for (a) $B = 1$ μG and (b) $B = 10$ G with $\vartheta_B = 30°$, $\varphi_B \in [0°, 360°]$. Different curves correspond to dashed (single scattering: SS), dot-dashed (disk integrated: DI), and dash-triple-dotted (LOS integrated). Black symbols mark $\varphi_B = 0°$ and 360°.

of the highest degree of anisotropic scattering, while the anisotropy decreases successively for the other two cases.

7. Conclusions

In the present paper we have derived the scattering matrix for the case of $J = 0 \rightarrow 1 \rightarrow 0$ $M1$ transitions in arbitrary-strength magnetic fields. For this purpose, we used the classical scattering matrix approach of Stenflo (1994, 1998) together with the classical damped magnetic dipole oscillator model of Casini & Lin (2002). This matrix describes various cases like Hanle, saturated Hanle, intermediate Hanle-Zeeman, and pure Zeeman regimes in a continuous way, hence the name Hanle-Zeeman scattering matrix. We also expressed the Hanle-Zeeman $M1$ scattering matrix in terms of the irreducible spherical tensors

(Landi Degl'Innocenti 1984) and the generalized profile functions (Landi Degl'Innocenti et al. 1991). We showed that this matrix is related to the scattering matrix for $E1$ transitions in a simple manner, involving only sign changes of some of the matrix elements. This could then allow for a straightforward generalization of the $M1$ scattering matrix to arbitrary $J_l \rightarrow J_u \rightarrow J_l$ scattering transition. The differences and similarities between the scattering matrix for $E1$ and $M1$ transitions were also illustrated through polarization diagrams.

For illustrations we considered scattering on the [Fe XIII] ion placed at a height h above the solar limb. We approximated the [Fe XIII] ion by a two-level atom model. In particular, we were interested in the [Fe XIII] 10747 Å line. We chose this particular line as it will be used for spectropolarimetric measurements in the solar corona by Aditya-L1 mission (Prasad et al. 2017). However, as demonstrated in Sahal-Bréchot (1977) and House (1977), the two-level atom approximation is insufficient when collisions are important. Indeed, they show that only when electron densities are lower than 10^7 cm^{-3}, the two-level atom approximation suffices to model the polarization profiles of [Fe XIII] 10747 Å line. For the electron density model considered by House (1977) and also this paper, this occurs at heights larger than 0.5 $R_\odot$ above the limb. However, the heights at which the transition from collision-dominated excitation to radiation-dominated excitation takes place depend on the electron density model and also on the spectral line under consideration (see Habbal et al. 2011). For example, electron densities in coronal holes may drop below 10^7 cm^{-3} around 0.2 $R_\odot$ above the limb (see Figure 2 of Doschek et al. 1997). Clearly, our formalism can be applied to those regions in the solar corona where radiative excitations dominate. Near the solar limb, where collisions cannot be neglected, one should resort to the density matrix formalism developed by the previous authors (House 1977; Sahal-Bréchot 1977; Casini & Judge 1999), which is limited to the saturated Hanle regime, however. Therefore we showed the behavior of the Stokes profiles emerging from a height $h = 0.5\,R_\odot$ above the solar limb. We considered different cases such as SS, integration over a cone of incident radiation from the photosphere (also called disk integration), and integration along the LOS for an atom in conditions typical of the solar corona. We have explored a broad range of field strengths and different field orientations. As expected, the [Fe XIII] 10747 Å line remains in the saturated Hanle regime for a rather wide range of field strengths. We also presented the frequency-integrated degree of linear polarization for different field distributions (such as radial and dipole fields). Furthermore, we studied the symmetry properties of the $M1$ scattering matrix through polarization diagrams.

For our studies we have varied the field strength from μG to kG ranges. However, only fields on the order of 1–30 G are expected in the solar corona (Lin et al. 2000). Magnetic fields as low as μG can be found in diffuse media such as the ISM, circumstellar regions, and supernova remnants (Yan & Lazarian 2006, Ferriére 2009; Reynolds et al. 2012). In these regions several forbidden lines are observed that in principle may respond to the μG field through the Hanle effect. Fields in the range of a few hecto-Gauss to kG are found in stellar atmospheres (Landstreet 2015). Indeed, the Hanle effect in allowed lines ($E1$ transitions) can be used as a tool to diagnose such stellar magnetic fields (see, e.g., Ignace et al. 2011; López Ariste et al. 2011; Bommier 2012; Manso Sainz & Martínez González 2012). As for the forbidden lines, they are also formed in the stellar winds, where field strengths as large as kG can be found (de la Chevrotiére et al. 2014). Our theoretical formalism may find application in modeling the polarization profiles of forbidden lines formed in the above-mentioned astrophysical contexts.

The authors would like to thank Prof. J. O. Stenflo for useful comments and suggestions on an early version of this paper. We thank an anonymous referee for constructive comments and suggestions that helped improve the paper.

References

Bommier, V. 1997, A&A, 328, 726
Bommier, V. 2012, A&A, 539, A122
Bommier, V., & Stenflo, J. O. 1999, A&A, 350, 327
Casini, R., & Judge, P. G. 1999, ApJ, 522, 524
Casini, R., & Lin, H. 2002, ApJ, 571, 540
Charvin, P. 1965, AnAp, 28, 877
de la Chevrotiére, A., St-Louis, N., & Moffat, A. F. J. 2014, ApJ, 781, 73
de Wijn, A. G., Socas-Navarro, H., & Vitas, N. 2017, ApJ, 836, 29
Dopita, M. A., Seitenzahl, I. R., Sutherland, R. S., et al. 2016, ApJ, 826, 150
Doschek, G. A., Warren, H. P., Laming, J. M., et al. 1997, ApJL, 482, L109
Ferriére, K. 2009, A&A, 505, 1183
Frisch, H. 2007, A&A, 476, 665
Gibson, S. E., Kucera, T. A., White, S. M., et al. 2016, FrASS, 3, 8
Habbal, S. R., Druckmüller, M., Morgan, H., et al. 2011, ApJ, 734, 120
House, L. L. 1972, SoPh, 23, 103
House, L. L. 1977, ApJ, 214, 632
Hyder, C. L. 1965, ApJ, 141, 1382
Ignace, R., & Brimeyer, A. 2006, MNRAS, 371, 343
Ignace, R., Hole, K. T., Cassinelli, J. P., & Henson, G. D. 2011, A&A, 530, A82
Jess, D. B., Reznikova, V. E., Ryans, R. S. I., et al. 2016, NatPh, 12, 179
Judge, P. G., & Casini, R. 2001, in ASPC 236, Advanced Solar Polarimetry-Theory, Observation and Instrumentation, ed. M. Sigwarth (San Francisco, CA: ASP), 503
Kraus, M., Fernandes, M. B., & de Araújo, F. X. 2010, A&A, 517, A30
Landi Degl'Innocenti, E. 1984, SoPh, 91, 1
Landi Degl'Innocenti, E., Bommier, V., & Sahal-Bréchot, S. 1991, A&A, 244, 391
Landi Degl'Innocenti, E., & Landolfi, M. 2004, Polarization in Spectral Lines (Dordrecht: Kluwer), LL04
Landstreet, J. D. 2015, in Proc. IAU Symp. 305, Polarimetry: From the Sun to the Stars and Stellar Environments, ed. K. N. Nagendra et al. (Cambridge: Cambridge Univ. Press), 12
Lin, H., & Casini, R. 2000, ApJ, 542, 528
Lin, H., Penn, M. J., & Tomczyk, S. 2000, ApJL, 541, L83
López Ariste, A., Asensio Ramos, R., & González Fernández, F. 2011, A&A, 527, A120
Manso Sainz, R., & Martínez González, M. J. 2012, ApJ, 760, 7
Newkirk, G. N., Jr., Dupree, R. G., & Schmahl, E. J. 1970, SoPh, 15, 15
Öhman, Y. 1929, MNRAS, 89, 479
Pierce, K. 2000, in Allen's Astrophysical Quantities, ed. A. N. Cox (4th ed.; New York: Springer), 355
Prasad, R., Banerjee, D., Singh, J., et al. 2017, CSci, submitted
Querfeld, C. W. 1982, ApJ, 255, 764
Reynolds, S. P., Gaensler, B. M., & Bocchino, F. 2012, SSRv, 166, 231
Sahal-Bréchot, S. 1974, A&A, 36, 355
Sahal-Bréchot, S. 1977, ApJ, 213, 887
Sampoorna, M., Nagendra, K. N., & Stenflo, J. O. 2007, ApJ, 670, 1485 (SNS07)
Stenflo, J. O. 1994, Solar Magnetic Fields (Dordrecht: Kluwer) (S94)
Stenflo, J. O. 1998, A&A, 338, 301 (S98)
Wood, R. W. 1905, PUSNO, 4, D116
Yan, H., & Lazarian, A. 2006, ApJ, 653, 1292
Zirin, H. 1976, Natur, 259, 466